S. Towfighian
Department of Mechanical Engineering,
University of Waterloo,
Waterloo, ON, N2L 3G1, Canada
e-mail: stowfigh@engmail.uwaterloo.ca

G. R. Heppler
e-mail: heppler@uwaterloo.ca

E. M. Abdel-Rahman[1]
e-mail: eihab@uwaterloo.ca

Department of Systems Design Engineering,
University of Waterloo,
Waterloo, ON, N2L 3G1, Canada

Analysis of a Chaotic Electrostatic Micro-Oscillator

The closed-loop dynamics of a chaotic electrostatic microbeam actuator are presented. The actuator was found to be an asymmetric two-well potential system with two distinct chaotic attractors: one of which occurs predominantly in the lower well and a second that visits a lower-well orbit and a two-well orbit. Bifurcation diagrams obtained by sweeping the ac voltage amplitudes and frequency are presented. Period doubling, reverse period doubling, and the one-well chaos through period doubling are observed in amplitude sweep. In frequency sweep, period doubling, one-well, and two-well chaos, superharmonic resonances and on and off chaotic oscillations are found.
[DOI: 10.1115/1.4002086]

1 Introduction

Chaos is a type of nonlinear vibration that is undesirable in the dynamic response of most systems; however, it has proven useful at the macroscale in structural health monitoring of aeroelastic systems [1–3], fault detection in roller bearings [4], and detection of corrosion [5]. The common useful characteristics in all these applications are the sensitivity of the chaotic response to variations in the structure properties and its capability as a detection mechanism.

In microscale, nonlinear responses, bistability, and chaos have been reported by researches in atomic force microscopy (AFM) [6–11] and electrostatic microelectromechanical system (MEMS) [12–22]. Chaos has been observed in tapping mode AFM via simulations and experiments [6–8]. An AFM probe consists of a microcantilever beam with a tip at its end in close proximity to the surface of a specimen. Lee et al. [9] found bistability in static response and hysteretic jumps in the frequency response when the distance of the tip and sample was less than 10 nm. The potential energy in the bistable region was an asymmetric two-well potential. They also found that frequency response at large amplitudes contained higher harmonics due to period doubling.

Ashhab et al. [7] reported chaotic vibrations when the AFM probe is driven near its natural frequency to tap the sample surface. They modeled the beam-tip-sample interaction accounting for the damping and forcing. They found a homoclinic orbit and used Melnikov's method to find how that orbit breaks up in the presence of perturbations leading to chaos. Experimental studies [10,11] have also reported chaos in AFM where it was observed and characterized using fractal and correlation dimensions, Lyapunov exponents, and noise iteration calculations. The reported chaos was "weak," containing strong periodic oscillation.

There are a few studies on the nonlinear response of electrostatic MEMS [20,21]. Rhoads et al. [20] studied the softening, hardening, and mixed behaviors for a fixed-fixed electrostatic microbeam. They assumed that damping and electrostatic forces are small and used perturbation methods to find the frequency response of the beam at small amplitudes away from dynamic pull-in. They specified ac and dc voltage ranges for stable and unstable vibrations of the undamped beam. Zhang et al. [21] studied softening in electrostatic microcantilever beam using a lumped model that had both electrostatic force and squeeze film damping. They reported period doubling bifurcations in their simulations.

A number of researches [16–19] have studied the dynamic instabilities in electrostatic actuators due to pull-in and snap-through. Krylov [17] studied the instability of the actuators for voltages above dynamic pull-in using a reduced order model including squeeze film damping. Applying a dc step input, he found that the Lyapunov exponent of the dynamic response is positive for voltages above dynamic pull-in indicating unstable vibrations. The squeeze film damping was found to be significant for the electrode vibrating close to the substrate.

Bistability in MEMS, the potential behavior for the creation of chaos, was analyzed for electrostatic actuators [16–19], paying more attention to static response than dynamic responses. Zhang et al. [16] investigated the static response of an arch-shaped beam that shows either snap-through and pull-in or only pull-in under electrostatic loading. The snap-through response led to bistability with a large amplitude response. Krylov et al. [18] extended the study of the static response of arch-shaped beams by finding the closed form of the initial elevation required for snap-through to happen. They investigated the effect of elevation on the differences between snap-through and pull-in voltages. Experimental results of the static response were in close agreement with the simulation results. Das et al. [9] derived the pull-in and snap-through voltages of arched beams using a model including the material and geometrical nonlinearities in finite element and boundary element methods. They simulated the dynamic pull-in and snap-through response without damping.

Chaos in electrostatic MEMS was first investigated by Bienstman et al. [12]. They developed an autonomous impact resonator by taking advantage of the pull-in instability in an electrostatic microbeam resonator without a separate control circuit. The frequent impact, which produced chaos, was created by driving the electrode at a voltage larger than the pull-in voltage. Through simulations they observed chaotic behavior in the system response. They also reported experimental evidence of period doubling.

Chaos has also been observed in noninterdigitated comb drive electrostatic actuators. Wang et al. [13] modeled it using a mass-spring system as a Duffing oscillator with a two-well potential field. Through simulations and experiments, they have shown chaotic oscillations in the two-well region of the system. As an extension to this work, De and Aluru [14] presented a model for the system including the electrostatic forcing, nonlinear stiffness, and squeeze film damping. They showed that even in the absence of the nonlinear mechanical and fluidic forces, the system had chaotic motion. Thus, the electrostatic forces were found to be the

[1]Corresponding author.

Contributed by the Design Engineering Division of ASME for publication in the JOURNAL OF COMPUTATIONAL AND NONLINEAR DYNAMICS. Manuscript received May 8, 2009; final manuscript received March 4, 2010; published online September 27, 2010. Assoc. Editor: Harry Dankowicz.

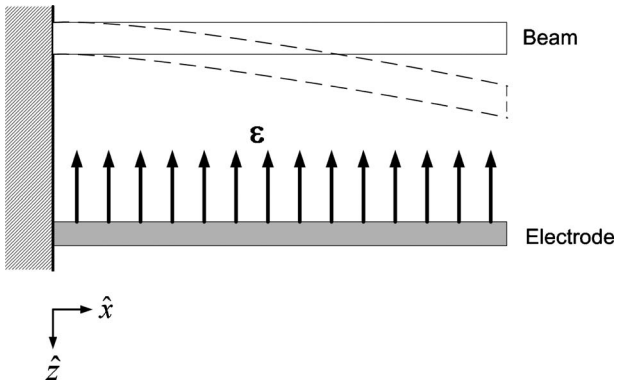

Fig. 1 Schematic of microbeam oscillator. The arrows indicate the electrostatic field.

primary mechanism producing chaos. The boundaries for chaotic motion in the amplitude-frequency space of the applied voltage were found both from experiments and from Melnikov's method by DeMartini et al. [15]. It was found that Melnikov's criteria underestimated the ac drive voltage threshold for chaos due to the fact that it predicted transient or attracting chaos and the experiments were showing only the boundary of attracting chaos.

Chaos has also been studied in a closed-loop feedback control system of an electrostatic actuator with capacitive sensing [22]. The open-loop micro-actuator had one stable equilibrium point throughout its operating range while the closed-loop system added another stable equilibrium point in a limited interval of the operating voltage, thus making the system bistable. Liu et al. [22] reported chaos and Hopf bifurcation in response of the electrostatic microcantilever beam to strong force disturbances using a lumped parameter model. Their goal was to avoid bistability and nonlinear dynamics.

This paper is focused on developing a nonlinear chaotic resonator that can be used for high resolution sensing. The goal is not to avoid nonlinear dynamic behavior but to employ it for achieving better resolution and sensitivity, which requires a thorough study of the complex nonlinear oscillations. In this work, nonlinear vibrations for the closed-loop feedback system by Liu et al. [22] is investigated in detail. The regions of the parameter space including controller parameters and actuation voltages for having bistability are explored and then bistability is used for the creation of chaos. Finally, bifurcation diagrams are presented that show the actuation ac voltage and frequency ranges required for chaotic vibrations.

2 Open-Loop System

The open-loop micro-actuator system consists of two electrodes that form a capacitor, one electrode is the cantilever beam on top and the other is the electrode underneath (Fig. 1). The applied voltage between the two electrodes creates an electrostatic force, the actuation force that moves the beam.

The steps taken in system modeling are as follows: (1) a partial differential equation representing the motion of a continuous microcantilever beam under electrostatic loading are formulated, (2) the distributed-parameter equation of motion is discretized using Galerkin's method with the mode shapes of a cantilever beam used as basis functions, and (3) the number of modes required to obtain convergence for the static deflection of the beam (pull-in profile) under electrostatic loading are determined.

The equation of motion for a damped cantilever beam in an electrostatic field is found, using the Euler–Bernoulli beam model, to be

Table 1 The electrostatic actuator parameters [22]

Parameter	Symbol	Value
Amplification factor	Ψ	1.5274 V
Controller gain	G	1
Density	ρ	2331 kg/m^3
Beam length	L	200 μm
Beam width	b	80 μm
Beam height	h	4.5 μm
Initial gap	d	3 μm
Nondimensional damping coefficient	μ	0.73
Quality factor	Q	4.817
Permittivity of air	ε	8.85×10^{-12} F/m
Modulus of elasticity	E	166 GPa
Controller damping	r	100

$$\rho A\frac{\partial^2\hat{w}(\hat{x},\hat{t})}{\partial\hat{t}^2}+EI\frac{\partial^4\hat{w}(\hat{x},\hat{t})}{\partial\hat{x}^4}+c\frac{\partial\hat{w}(\hat{x},\hat{t})}{\partial\hat{t}}=\frac{\varepsilon_0 bV_{\mathrm{dc}}^2}{2(d-\hat{w}(\hat{x},\hat{t}))^2} \tag{1}$$

where $\hat{w}(\hat{x},\hat{t})$ is the deflection of the beam in the $\hat{z}$ direction, $\hat{x}$ is the coordinate along the beam length, and $\hat{t}$ is time. The linear viscous damping coefficient per unit length c is used to account for damping losses due to the beam motion through air, V_{dc} is the applied dc voltage, and the other parameters are defined in Table 1. The right hand side represents the electrostatic force per unit length. Following Nayfeh et al. [23], we multiply both sides by $(d-\hat{w})^2$ and introduce the following nondimensional parameters:

$$x=\frac{\hat{x}}{L},\quad w=\frac{\hat{w}}{d},\quad t=\frac{\hat{t}}{T} \tag{2}$$

where L is the beam length, T is

$$T=\sqrt{\frac{\rho AL^4}{EI}} \tag{3}$$

to rewrite the equation of motion (1) in nondimensional form as

$$\frac{\partial^2 w}{\partial t^2}(1-w)^2+\frac{\partial^4 w}{\partial x^4}(1-w)^2+\mu\frac{\partial w}{\partial t}(1-w)^2=\alpha V_{\mathrm{dc}}^2 \tag{4}$$

where

$$\mu=\frac{cL^4}{EIT} \tag{5}$$

and

$$\alpha=\frac{\varepsilon_0 bL^4}{2EId^3} \tag{6}$$

representing the electromechanical coupling coefficient. The solution to Eq. (4) is sought using Galerkin's method with a trial function of the form

$$w(x,t)=\sum_{n=1}^{M}\Phi_n(x)q_n(t) \tag{7}$$

where $\Phi_n(x)$ is the nth cantilever beam mode shape normalized with respect to the beam-tip modal deflection so that $\Phi_n(1)=1$, q_n is the nth generalized coordinate, and M is the number of modes (degrees of freedom) considered in the expansion. Using Galerkin's method and separation of variables [24], one gets a set of M ordinary second-order differential equations in terms of q_n, where $n=1,\ldots,M$. For a one-mode approximation, the equation is

$$(\ddot{q}_1+\mu\dot{q}_1+\omega_1^2 q_1)(1+c_1q_1+c_2q_1^2)=c_3\alpha V_{\mathrm{dc}}^2 \tag{8}$$

where overdot means derivative with respect to time, ω_1 is the first natural frequency of the beam, and c_1, c_2, and c_3 are found after applying Galerkin's method.

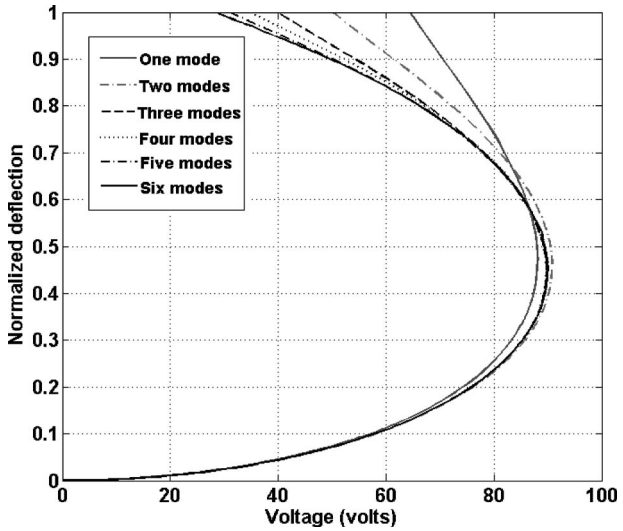

Fig. 2 Nondimensional deflection of the beam tip versus voltage V_{dc}

2.1 Static Analysis. The static equilibrium equations of the beam-tip deflection are obtained for the multidegree-of-freedom model by setting the time derivatives to zero in the equation of motion. For the multi-DOF model, the result is a set of M cubic polynomial equations in terms of q_n, $n=1,\ldots,M$ and their products. Solving these equations yields the beam-tip deflection

$$w_1 = w(1) = \sum_{n=1}^{M} q_n \tag{9}$$

For a one-mode approximation, the equilibrium equation is

$$\omega_1^2(q_1 + c_1 q_1^2 + c_2 q_1^3) = c_3 \alpha V_{dc}^2 \tag{10}$$

The solution of the equilibrium equation for the nondimensional beam-tip deflection as a function of dc voltage is shown in Fig. 2. The pull-in point, where the slope of the deflection versus voltage becomes infinite, is predicted to occur at 45% of the gap between the electrode and the beam, which is larger than the 33% predicted by using a single DOF lumped parameter model [25].

The local stability of the two branches of equilibrium points below and above the pull-in point is examined by finding the eigenvalues of the Jacobian matrix evaluated at the equilibrium point. It is found that the real parts of the eigenvalues of the lower branch are always negative (stable), while one of the eigenvalues of the upper branch is always positive (unstable). At the pull-in point, one of the eigenvalues is zero, indicating a saddle-node bifurcation. For example, at $V_{dc}=75$ V and using the one-mode model, the eigenvalues at the lower equilibrium point $w_1=0.2$ are $(-0.36 \pm 2.8i)$. At the upper equilibrium point $w_1=0.83$, the eigenvalues are (0.31) and (-4.44). Therefore, the lower equilibrium is a stable equilibrium, while the upper equilibrium is an unstable equilibrium. Furthermore, the nondimensional natural frequency of the stable equilibrium point (the imaginary part of the eigenvalues) is smaller than that of the straight beam, 2.8 versus 3.5158, which indicates a decrease in linear stiffness due to the electrostatic force.

The effect of the number of modes used in the Galerkin approximation (number of degrees of freedom) on convergence is shown in Fig. 2. Using the first three mode shapes, asymptotic convergence is obtained over the full extent of the lower branch of equilibrium solutions; six modes are required for the solution to converge on the upper branch.

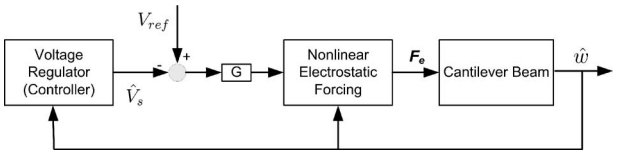

Fig. 3 Closed loop system schematic

3 Closed-Loop System

The control law introduced by Liu [22] is used to create chaos in the system. The creation of chaos is made possible by using the controller to create an additional stable potential well in the system. The schematic closed-loop system is shown in Fig. 3. The cantilever beam is actuated by the electrostatic forcing, which is controlled by the voltage regulator (controller). The voltage regulator is an electronic circuit designed to have the same function as the capacitive sensor in Ref. [22]. In Fig. 3, V_{ref} is the reference input voltage, $\hat{V}_s$ is the controller output voltage, and G is a gain. The voltage applied between two electrodes is $G(V_{ref}-\hat{V}_s)$ that creates the electrostatic forcing on the cantilever beam and is proportional to $F_e \propto G^2((V_{ref}-\hat{V}_s)^2/(d-\hat{w})^2)$.

The equations for the closed-loop system are obtained by replacing V_{dc} in Eq. (4) with a voltage difference between a reference and the controller output. Therefore, the equation of motion becomes

$$\ddot{w}(1-w)^2 + w^{(4)}(1-w)^2 + \mu\dot{w}(1-w)^2 = G^2(V_r - V_s)^2 \tag{11}$$

where V_s and V_r are voltages normalized according to

$$V_r = \sqrt{\alpha} V_{ref} \quad \text{and} \quad V_s = \sqrt{\alpha}\hat{V}_s \tag{12}$$

The differential equation for the controller voltage (V_s) is [22]

$$\dot{V}_s = -r\left(V_s - \frac{w(1)}{1-w(1)}\Psi\sqrt{\alpha}\right) \tag{13}$$

where Ψ and r are referred to as the amplification factor and controller damping, respectively. Equations (11) and (13) are treated by using Galerkin's method with the trial function from Eq. (7), similar to Sec. 2.1. For a one-mode approximation, we get

$$\begin{aligned}(\ddot{q}_1 + \mu\dot{q}_1 + \omega_1^2 q_1)(1 + c_1 q_1 + c_2 q_1^2) &= c_3 G^2(V_r - V_s)^2 \\ \dot{V}_s &= -r\left(V_s - \frac{q_1}{1-q_1}\Psi\sqrt{\alpha}\right)\end{aligned} \tag{14}$$

3.1 Static Analysis. To investigate the static response of the closed-loop system, we obtain the static equilibrium equations from Eq. (14) by setting the time derivatives to zero. Consequently, V_s is found to be

$$V_s = \frac{q_1}{1-q_1}\Psi\sqrt{\alpha} \tag{15}$$

Substituting Eq. (15) into the first equation of Eq. (14) yields

$$\omega_1^2 q_1(1 + c_1 q_1 + c_2 q_1^2) = c_3 \alpha G^2\left(V_{ref} - \frac{q_1}{1-q_1}\Psi\right)^2 \tag{16}$$

which simplifies to

$$q_1^5 + a_4 q_1^4 + a_3 q_1^3 + f_2(V_{ref}, G)q_1^2 + f_1(V_{ref}, G)q_1 + f_0(V_{ref}, G) = 0 \tag{17}$$

where a_3, a_4 are constants and the $f_n(V_{ref}, G)$ are the second-order polynomials in input voltage V_{ref} and controller gain G. The solution to Eq. (17) is obtained numerically for a given V_{ref}.

Figure 4 depicts the nondimensional beam-tip deflection versus voltage V_{ref} when one to five modes are used in the Galerkin

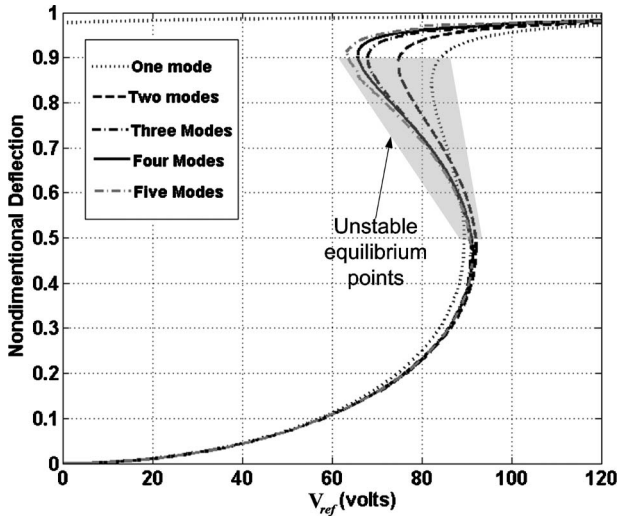

Fig. 4 Nondimensional deflection of the beam tip versus voltage, V_{ref}, for the closed-loop system

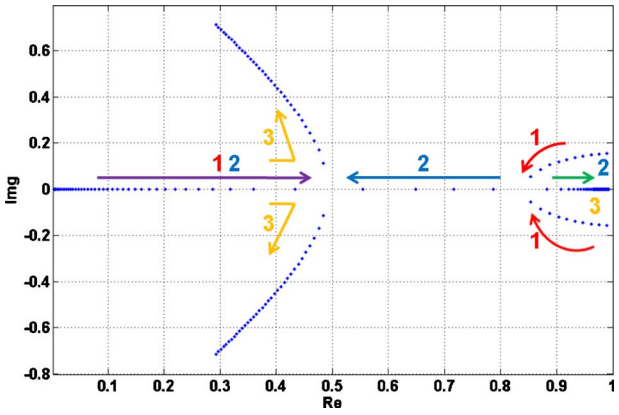

Fig. 5 Roots of the equilibrium equation q_1 in complex plane

expansion. The profile has two turning points, which have infinite slopes, and which are saddle-node bifurcation points. Once we increase the voltage, two fixed points appear at the first turning point, and two fixed points disappear at the second turning point showing saddle-node bifurcation. The stability of the fixed points is investigated in Sec. 3.2.1. As can be deduced from Fig. 4 and from the stability analysis of the fixed points, part of the profiles between the two turning points (covered by a gray area in the figure) is the location of unstable equilibrium points at a specified voltage. Above and below the shaded region on the profiles are the locations of the stable equilibrium points. There also exists a line of fixed points close to unity, which, with its close proximity to pull-in, is outside our interest in this study.

Increasing the number of mode shapes widens the voltage range between the two stable parts of the curve by moving the first bifurcation point to a lower voltage. In the bistability region, the upper equilibrium point is larger for models with a higher number of modes, meaning that for a certain amount of forcing, models with more modes deflect more (softening effect). Similarly, for a certain deflection amount e.g., 0.9, models with fewer modes need more voltage to reach that level of deflection. This effect shows the system is more flexible than would be indicated by using a single DOF model.

Convergence on the lower branch of solutions in Fig. 4 is achieved using the first two mode shapes only. For the middle and upper branches, convergence is achieved using the first five modes except in the vicinity of the first turning point. Overall a three-mode-model shows reasonable accuracy across the full voltage range.

Another way of presenting the roots of the equilibrium Eq. (17) is in the complex plane, as depicted in Fig. 5. The arrows show the direction of increasing voltage V_{ref}. Number 1 shows the location of the roots for the region of voltages less than 65 V, number 2 refers to region of voltages between about 65 V and 90 V, and number 3 refers to voltages higher than 90 V in Fig. 4. From Fig. 5, it can be deduced that by increasing the voltage, in region 1, the two complex roots on the right side move leftward and approach the real axis and the other real root on the left is moving on the real axis toward the right. As the voltage is increased in region 2, the two complex roots on the right side join on the real axis and move in two different directions, while the third root on the left side continues moving to the right along the real axis. So in this region, we get three real roots that correspond to three equilibrium positions. Subsequently increasing the voltage in region 3 results in one real root continuing to move to the right along the real axis and the other two roots, those that are converging on one another, ultimately meeting and bifurcating into the imaginary parts of the complex plane. The same results can also be obtained for an actuator with different dimensions by adjusting the controller gain G. Since α is a function of dimensions (Eq. (6)) and according to Eq. (16), it is the product of $G^2\alpha$ that determines the location of the polynomial roots.

The size of bistability region can be adjusted by the parameters of controller gain G and amplification factor Ψ according to Eq. (16) as all other coefficients are fixed because they are either function of dimensions (e.g., α) or the Galerkin coefficients (e.g., c_1, c_2, c_3). The effect of controller gain G on the size of the bistability region is depicted in Fig. 6. At a critical gain value, the bistable region vanishes. For gain values larger than 3, the two turning points change to an inflection point. This point is a codimension 2 bifurcation, cusp point, in the parameter space of voltage V and gain G where a triple repeated root of the polynomial appears. This bifurcation is shown in Fig. 7. The solid lines show the location of the saddle-node bifurcation points. The intersection of the two solid lines is the location of the cusp point, beyond which the system has one equilibrium point. For the system to be bistable, the controller gain has to be less than the threshold defined by the cusp point. As shown in Fig. 6, the smaller the gain is, relative to the threshold, the larger the voltage range for bistability is. One of the main findings is also achieved here for gains larger than the threshold ($G=4$) shown, which demonstrates that the system can be stable for the whole gap distance. However, the

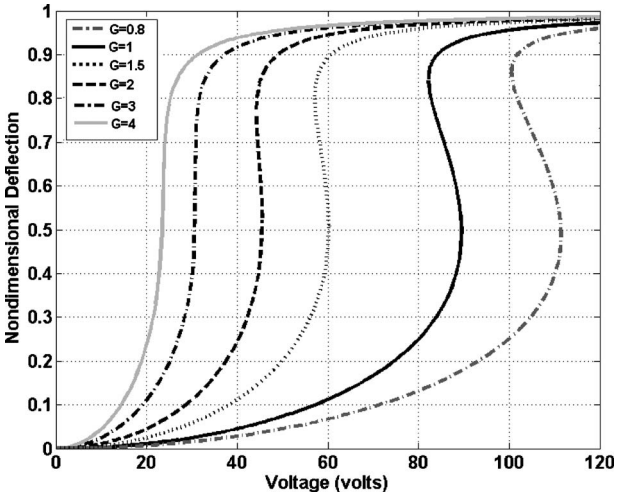

Fig. 6 Effect of the controller gain G on the static deflection versus voltage, V_{ref}, curve

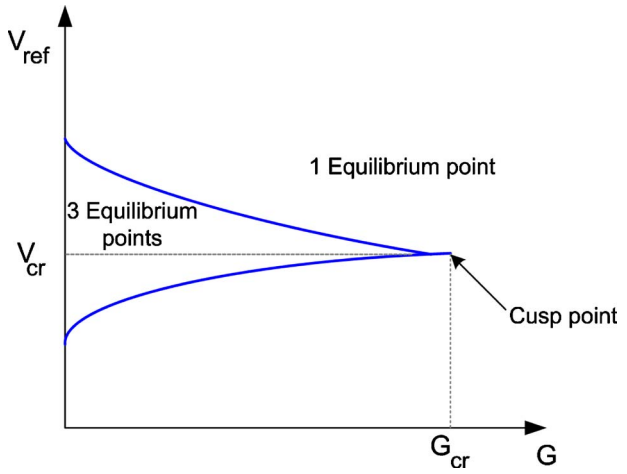

Fig. 7 Stability diagram in the parameter space of controller gain, G, and voltage, V_{ref}

dynamic results in Sec. 3.2.2 show the system is single stable for 83% of the gap and beyond that pull-in happens because of the presence of the upper saddle.

The bistability threshold, which classifies the system behavior, is identified by finding the triple repeated root of Eq. (17), i.e., by solving

$$F(q_1) = (q_1 - p_0)^3(q_1^2 + p_1 q_1 + p_2) = 0 \tag{18}$$

where p_0 is the triple root. The first and second derivatives with respect to q_1 also vanish at the triple root:

$$\left.\frac{dF}{dq_1}\right|_{q_1=p_0} = 0 \quad \text{and} \quad \left.\frac{d^2F}{dq_1^2}\right|_{q_1=p_0} = 0 \tag{19}$$

Solving Eqs. (18) and (19) numerically results in the coordinates of the cusp point (V_{ref}, G) and the triple real root of p_0. The threshold of bistability was found to be $G_{cr}=3.471$ and $V_{cr}=26.965$ V at the nondimensional deflection $q_{cr}=p_0=0.626$.

The other parameter affecting the size of bistability region is the amplification factor Ψ that can tune both the voltage range as well as the deflection range for bistability. Equation (16) indicates that increasing Ψ decreases the magnitude of the electrostatic force, helping the spring force to bring the system back to equilibrium and lower deflections. This is demonstrated in Fig. 8 using a one-mode approximation for a controller gain of $G=0.8$. Figure 8 shows that increasing the amplification factor Ψ moves the upper equilibrium away from pull-in, which makes the system safer to operate. On the other hand, the disadvantage of increasing Ψ is

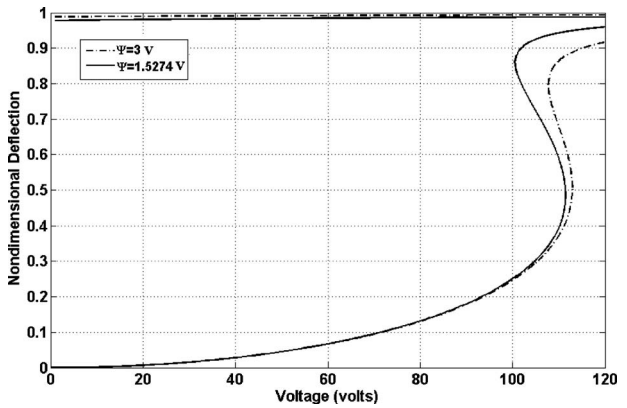

Fig. 8 Effect of amplification factor, Ψ, on static pull-in graph for $G=0.8$

Table 2 Eigenvalues for the fixed points at $V_{ref}=110$ V in Fig. 8 for $G=0.8$, $\Psi=3$ V

q_1	Eigenvalue 1	Eigenvalue 2
0.37	$-0.37-1.98i$	$-0.37+1.98i$
0.68	1.60	−2.33
0.864	$-0.37-4.45i$	$-0.37+4.45i$
0.985	61.17	−61.90

that the voltage range for the bistability decreases from 9 V for $\Psi=1.527$ V to 4.5 V for $\Psi=3$ V. Therefore, the controller gain G and the amplification factor Ψ need to be balanced to obtain a wide bistable region at deflection values far from pull-in. By choosing $G=0.8$ and $\Psi=3$ V, we obtain a reasonable voltage range for bistability of 4.5 V and an upper stable equilibrium that is less than %90 of the gap. Henceforth, we will adopt these values for the controller gains in conjunction with system parameters in Table 1 for the dynamic analysis of the bistable system.

3.2 Dynamic Analysis. Here the stability of the fixed points will be examined and then the dynamic responses are presented using a one-mode-model. The use of multiple modes to study the dynamic response was examined in a previous work [24]. It was shown that using the first three mode shapes in the model has the same qualitative dynamic behavior as using the first mode shape only. The difference is that the response of the three mode shape model features small oscillations on top of the phase portrait of the first mode shape. Due to its extensive computational time, a one-mode-model is used in this study. To analyze the closed-loop dynamics after adding the controller, first the state space equations are derived. Derivation is performed by discretizing Eqs. (11) and (13) using Galerkin's method. Using the first mode approximation, the resulting two differential equations would be in terms of q_1, the normalized beam-tip deflection for a single mode. Letting $y_1=q_1$, $y_2=\dot{q}_1$, and $y_3=V_s$, the system state space equations become

$$\begin{aligned} \dot{y}_1 &= y_2 \\ \dot{y}_2 &= -\mu y_2 - \omega_1^2 y_1 + \frac{c_3 G^2 (V_r - y_3)^2}{1 + c_1 y_1 + c_2 y_1^2} \\ \dot{y}_3 &= -r\left(y_3 - \frac{y_1}{1-y_1}\Psi\sqrt{\alpha}\right) \end{aligned} \tag{20}$$

For the dynamic analysis, the reference voltage, V_{ref}, will include a dc and an ac component so that the nondimensional reference voltage V_r is

$$V_r = \sqrt{\alpha} V_{ref} = \sqrt{\alpha}(V_{dc} + V_{ac}\cos(\omega t)) \tag{21}$$

where ω is the nondimensional circular frequency of excitation, and V_{ac} and V_{dc} are the ac and dc voltages, respectively.

3.2.1 Stability of Fixed Points. To determine the stability characteristics of the fixed points, Eq. (20) is linearized about an equilibrium point. Equation (15) is used in Eq. (20) to reduce the third order system to a second-order system. The eigenvalues of the Jacobian of the second-order system are then found at a given voltage for the corresponding static deflection. Table 2 shows the eigenvalues for the fixed points at input voltage, $V_{ref}=110$ V (Fig. 8). Only four roots of Eq. (17) are listed in Table 2 since the fifth root is aphysical with a value greater than 1. The first and third fixed points are stable foci, whereas the second and fourth fixed points are saddles.

The eigenvalues of the stable foci also reveal the magnitude of the natural frequency. In Table 2, the nondimensional frequencies for the first and third fixed points are 1.97 and 4.45, respectively. Since the canonical frequency for the undeflected cantilever beam

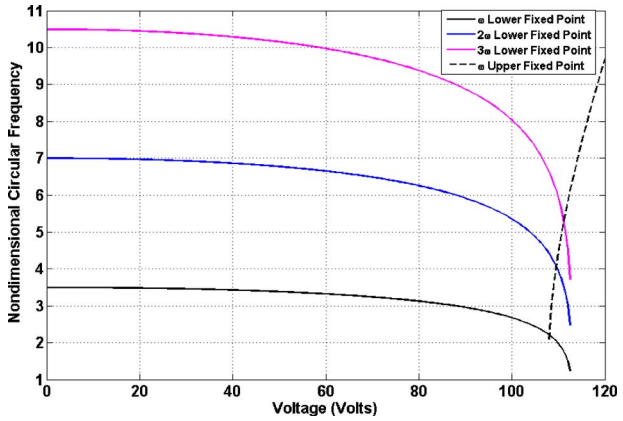

Fig. 9 Nondimensional circular frequency versus input voltage V_{ref}

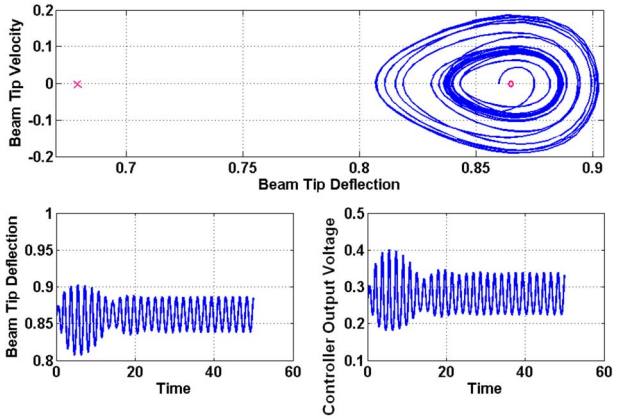

Fig. 11 The phase portrait, beam-tip deflection w_1 and controller output voltage, V_s, for $\mu=0.7$, $\omega=3.5158$, $V_{ac}=0.7$ V, and the initial condition ($q_1=0.86$, $\dot{q}_1=0$, $V_s=0.266$). The small circle and the cross show the location of the stable focus and saddle, respectively.

is 3.5158 (corresponding to 153.3 kHz), decreasing the frequency at the lower stable equilibrium indicates a linear softening effect of the electrostatic forces and increasing the frequency at the upper stable equilibrium point reveals a linear hardening effect of the controller. Figure 9 shows the nondimensional frequency obtained for the lower and upper stable equilibrium points using a one-mode approximation. It is interesting to note that in the bistability region [108–112.5 V], the system has a distinct fundamental natural frequency for each equilibrium point shown with black lines. In this graph, doubled and tripled natural frequencies of the lower equilibrium are also shown with blue and magenta lines, respectively; their intersections with the dashed black line reveal the possible interaction between the two equilibrium points. That is, once we excite the upper equilibrium at its natural frequency at those intersections, it can excite the lower one at its subharmonics.

3.2.2 Dynamic Response Results. The dynamic response of the system is first studied for the single stable system mentioned in Sec. 3.1 for a controller gain larger than the threshold value, then the analysis for the bistable system follows, which will be used for the creation of chaos. Results are obtained by numerically solving Eq. (20) using long time integration.

For the single stable system with the static profile of Fig. 6 and a gain of $G=4$, Fig. 10 depicts the phase portrait and the time series of the beam deflection both converging to the equilibrium point at 0.8309 of the gap. The graph is drawn for the maximum $V_{dc}=26.2$ that the system can have one stable point. Increasing the voltage makes the top electrode pull-in to the bottom electrode and the system loses its stability. The continuous stable solution enables actuation up to 83% of the initial gap higher than 60% achieved by Lu and Fedder [26].

To create chaos for the bistable system, one needs to choose the operating voltage from the bistability region because outside this region only periodic orbits are observed and as these orbits grow (by increasing the voltage) pull-in happens. We set the dc voltage to $V_{dc}=110$ V with $G=0.8$ and $\Psi=3$ V for all dynamic results of the bistable system from this point forward. Figures 11 and 12 show the dynamic response of the system, starting from an initial condition in the vicinity of the upper equilibrium point, in the bistability region for $V_{ac}=0.7$ V and $V_{ac}=0.9$ V, respectively. The normalized controller output voltage amplitude (V_s) is found to be a maximum of 0.5 in the two cases, this value, when divided by $\sqrt{\alpha}=0.014$, yields 35.7 V. Figure 11 shows a limit cycle around the upper equilibrium point in the upper potential well. Figure 12 shows the boundaries of the upper potential well. As the operating ac voltage is increased from 0.7 V to 0.9 V, the orbit becomes too large for the upper well, touches the stable manifold of the saddle, and escapes to the lower well on a small limit cycle around the lower equilibrium point. The size of the lower-well orbit at $V_{ac}=0.9$ V is smaller than the size of the upper well orbit at $V_{ac}=0.7$ V, 0.02 versus 0.05, which indicates that the lower potential well is deeper than the upper well. When the orbit escapes the

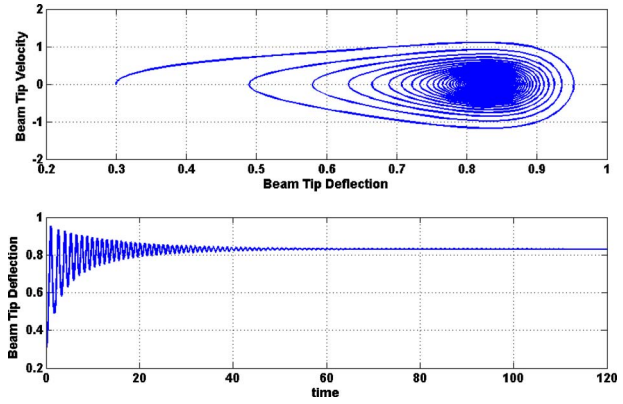

Fig. 10 The nondimensional phase portrait and beam deflection, V_s, for system parameters of $G=4$, $\Psi=1.5274$ V, $r=100$, $\mu=0.73$, $V_{ac}=0$ V, $V_{dc}=26.2$ V, and initial condition of ($q_1=0.3$, $\dot{q}_1=0$, $V_s=0.009$)

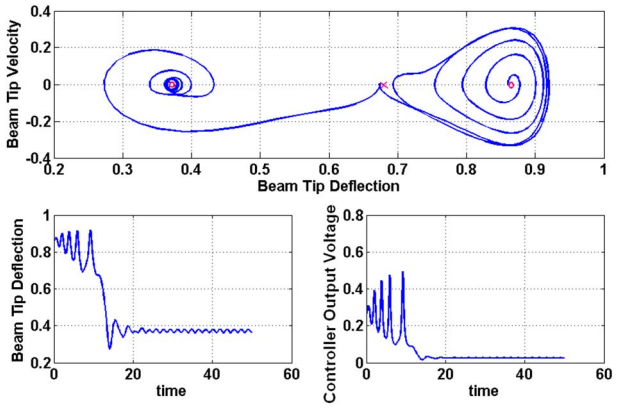

Fig. 12 The phase portrait, beam-tip deflection w_1, and normalized controller output voltage, V_s, for system parameters of $\mu=0.7$, $\omega=3.5158$, $V_{ac}=0.9$ V, and initial condition of ($q_1=0.86$, $\dot{q}_1=0$, $V_s=0.266$)

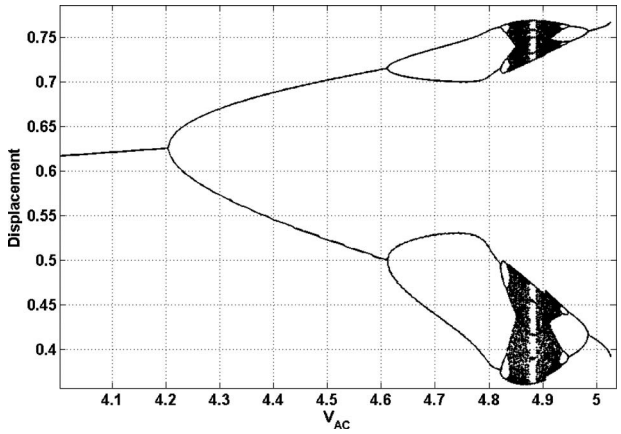

Fig. 13 Bifurcation diagram constructed from a force sweep V_{ac} at fixed nondimensional natural frequency of lower well ω_l =1.98

upper well to the lower one, it never comes back and it keeps oscillating in the lower well within a small limit cycle. Now that the asymmetry in the potential wells is known, we examine how to create chaos both in one and two potential wells.

3.2.3 Force Sweep. We sweep the amplitude of the harmonic excitation voltage V_{ac} while holding the excitation frequency fixed at ω_l=1.98, the nondimensional natural frequency of the lower equilibrium, to obtain the bifurcation diagram of the actuator shown in Fig. 13. The solution to the dynamic system is found for a duration of 4000 periods of excitation, and the data for the last 128 periods are presented. Poincaré sections are taken by sampling the data at the period of excitation starting from the maximum displacement. The amplitude of excitation starts at 4 V, and once we increase it, the amplitude of response increases until we observe period doubling, and periods 2 and 4 and higher appear in one well, as illustrated in Fig. 14. Results are shown for the last 100 time units after the transients disappeared at 4 V, 4.4 V, and 4.7 V. Multiple periods are recognized by the fast Fourier transform (FFT) plot of the beam-tip displacement time series profile. In the FFT of period 2 (Fig. 14 middle), in addition to the peaks at the period one (top), we see the appearance of middle peaks. This trend is also seen in the FFT of period 4 (bottom).

Following the period doubling in Fig. 13, chaos happens in one well very close to period 8 and the attractor size keeps increasing. Chaos occurs in two bands, one around the lower equilibrium and the other around the middle saddle. The size of the lower band is

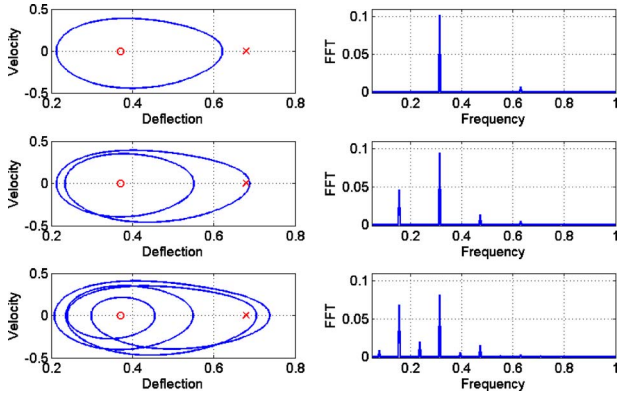

Fig. 14 The phase portraits and fast Fourier transforms using a one-mode model, the system parameters μ=0.7, ω=1.98. (Top) Periodic V_{ac}=4.1 V. (Middle) Period two V_{ac}=4.4 V. (Bottom) Period four V_{ac}=4.7 V.

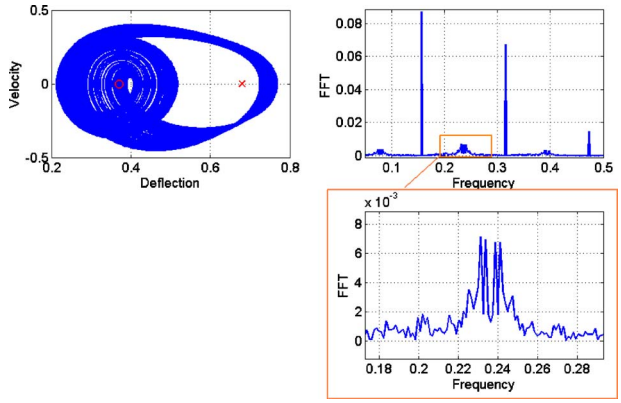

Fig. 15 The phase portrait and fast Fourier transform of chaotic oscillation. The system parameters are μ=0.7, ω=1.98, and V_{ac}=4.861 V.

larger than the upper band. The phase portrait of the chaotic attractor is shown in Fig. 15 for the voltage of 4.861 V. The two band attractor crosses the zero velocity axis at four solid thick areas, two of which are joined on the left side. The Poincare section at periods of excitation in Fig. 13 records the points in Fig. 15 at the intersections of two solid areas on the right with the zero velocity axis around 0.45 and 0.75. The difference in the attractor band size is obvious by comparing the thickness of the solid lines about 0.45 and 0.75 of the gap. A FFT plot in Fig. 15 is zoomed in by the rectangle area that reveals the broad range of frequencies present only in a chaotic type of vibration. The actuator oscillates primarily in the lower well with brief excursions into the upper well. Comparing these results to the reports of Nayfeh et al. [27] and Najar et al. [28] of period doubling followed by pull-in in a single-well actuator, we conclude that the upper well functions as a barrier against pull-in in this case. In other words, once the energy becomes large, the orbit passes the potential hump to the upper well that consumes its energy and therefore protecting it from pull-in.

Inside the chaotic attractor presented in Fig. 13, there also exists a period of 10 window for the excitation voltage range of [4.875–4.888] (Fig. 16). Consequently after period 10, chaos follows and the attractor size keeps decreasing until it disappears through a reverse period doubling ending in a period 2 orbit. This orbit disappears at V_{ac}=5.02 V where pull-in occurs. No stable orbits exist beyond this point.

3.2.4 Frequency Sweep. We also found a two-well chaotic solution by sweeping the frequency of excitation. The complete pic-

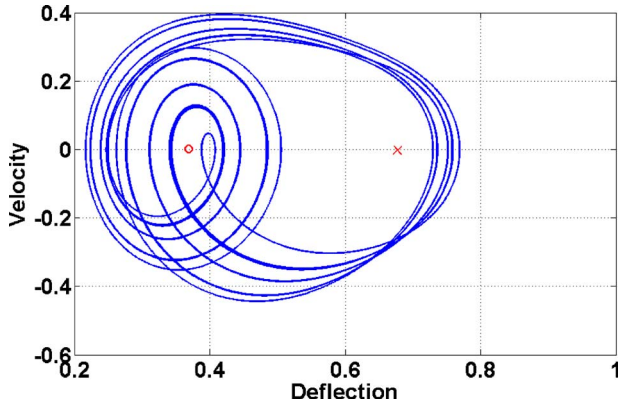

Fig. 16 Phase portrait of period 10 in one well once the amplitude of excitation V_{ac}=4.883 and the nondimensional frequency of excitation ω is 1.98

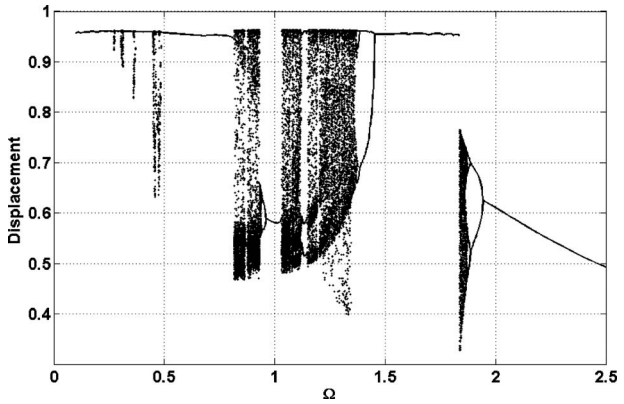

Fig. 17 Bifurcation diagram sweeping the frequency of excitation at fixed V_{ac} of 4 V

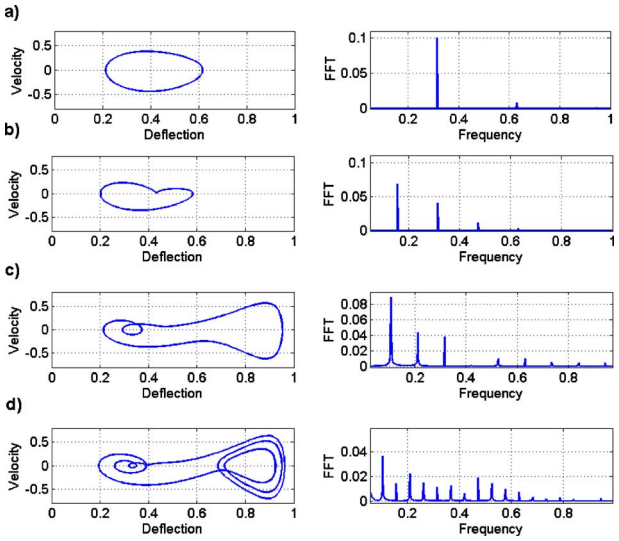

Fig. 18 Phase portraits and FFT for the periodic orbit at the (*a*) natural frequency of the lower equilibrium $\Omega=\omega_l=1.98$, (*b*) superharmonic resonance of order two at $\Omega=\omega_l/2=0.99$, (*c*) superharmonic resonance of order three at $\Omega=\omega_l/3=0.66$, and (*d*) superharmonic resonance of order six at $\Omega=\omega_l/6=0.33$

ture of the bifurcation diagram for sweeping the frequency of excitation is given in Fig. 17. Above the natural frequency of the lower equilibrium (at 37% of the gap (Table 2)), 1.98, and an ac amplitude of 4 V, there only exist lower-well periodic orbits. Below it, once we decrease the frequency, first period doubling happens, which develops into the primarily one-well chaotic attractor. The bifurcation diagram shows the softening behavior typical to electrostatic actuators. The one-well chaos disappears by decreasing the frequency and changes to a periodic two-well solution. Subsequently at a frequency of $\Omega=1.45$, a period doubling cascade happens to the two-well orbit culminating in a two-well chaotic attractor. It continues while decreasing the frequency until it encounters a window of period three orbits in the frequency range [1.122–1.143]. The chaotic attractor disappears to be replaced by a period 1 orbit in the lower well at $\Omega=1.031$. In this range, the superharmonic resonance of order 2 at $\Omega=\omega_L/2$ strengthens the regularity of the actuator oscillations, thereby eliminating the chaotic attractor and replacing it with a periodic orbit. A weaker softening behavior is also observed around this frequency that converts to a period doubling cascade and takes the orbit back to a two-well chaos. The two-well chaos changes to superharmonic orbits at the frequency of $\Omega=0.817$ that continues to exist down the frequency with occasional chaotic oscillations. The disappearance of one-well periodic orbits at low excitation frequencies can be explained by considering the total energy of the system. At low excitation frequencies, the velocity, which is proportional to Ω, is low and the kinetic energy is low, so the potential energy has to absorb the orbit energy via large displacement over the orbit solution. As the excitation frequency increases, the velocity increases and absorbs most of the energy and consequently the orbit displacement shrinks leading to one-well periodic orbit.

In studying the dynamic behavior of the system by changing the frequency, we also observed superharmonic resonances of order 2, 3, and 6 of the natural frequency of the lower equilibrium. In Fig. 18, we show the phase portraits and the FFT of these orbits. The first resonant peak in Fig. 18(*a*) splits to two, three, and six in parts (b), (c), and (d), respectively, indicating the aforementioned superharmonic resonances.

To illustrate the chaotic oscillation observed, the phase portraits, and the Lyapunov exponents of the one-well chaotic attractor at $\Omega=1.84$, and the two-well attractor at $\Omega=1.081$ are shown in Figs. 19 and 20, respectively. The one-well attractor is fully developed and located primarily in the lower well with occasional excursions over the saddle. The two-well attractor consists of oscillations in the lower well and between the two wells with no exclusive oscillations in the upper well. The leading Lyapunov exponents are obtained by tracking the distance between two trajectories starting from initial conditions at a distance $d_0=10^{-9}$ from each other in phase space. The overtime evolutions of the logarithm of the distance d_1 normalized with respect to the initial distance are illustrated in Figs. 19(*b*) and 20(*b*) by the dotted lines and their moving averages are shown by the solid lines. The slope of the solid curve during the chaotic attractor expansion is the leading Lyapunov exponent. It is found to be positive for both attractors proving that they are indeed chaotic [29].

4 Summary and Future Work

A chaotic micro-actuator is developed by adding a voltage regulator (controller) to an electrostatic microcantilever beam actuator. Nonlinear elements present in the model include a voltage regulator and the electrostatic forcing. Static and dynamic responses of the nonlinear system are explored. The static response shows that by adjusting the controller gains, the system can be configured as either a stable single-valued actuator or a bistable actuator. The single-valued system is a stable smoothly varying actuator with a stroke of as much as 83% of the capacitor gap, much larger than the pull-in deflection of 45% of the open-loop electrostatic actuator. The bistable system, on the other hand, is used to create a chaotic actuator. We found that bistability was necessary but not a sufficient condition for chaos. The excitation ac voltage amplitude and frequency had to be chosen properly to obtain chaos.

Both one-well and two-well chaotic attractors have been found. The excitation parameter boundaries of the chaotic attractors were obtained using force and frequency sweeps. Period doubling, reverse period doubling cascades, and a banded one-well chaotic attractor were obtained in the force sweep. Beyond a threshold of ac voltage amplitude, pull-in occurs and precludes bounded motion. In addition, sweeping the frequency of excitation, we observed one-well and two-well chaotic attractors. A softening-type nonlinearity beside superharmonic resonances are also observed in the response as we decrease the excitation frequency below the natural frequency.

Our future work includes implementing the system by building an electronic circuit on a print circuit board for the voltage regulator (controller) that functions according to Eq. (13). The velocity of the microbeam will be measured by a laser interferometry vibrometer and the corresponding analog signal will be fed to the controller circuit. The controller output voltage will be adjusted

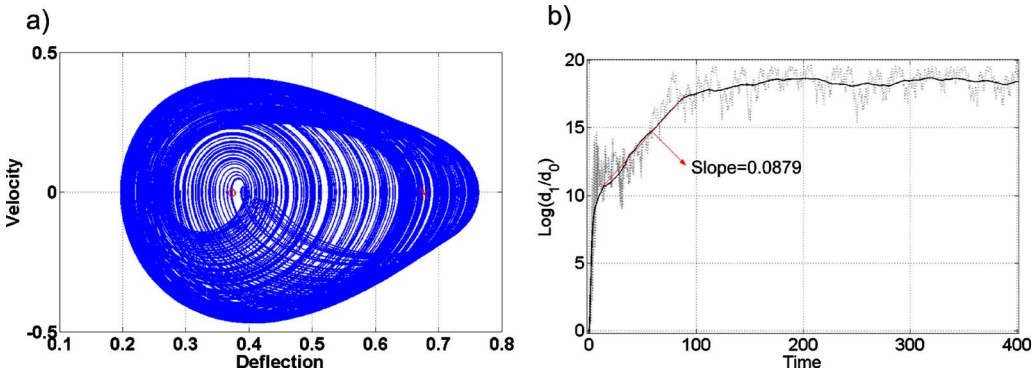

Fig. 19 (*a*) Phase portrait and (*b*) Lyapunov exponent of the one-well chaotic attractor when $V_{ac}=4$ and $\Omega=1.84$

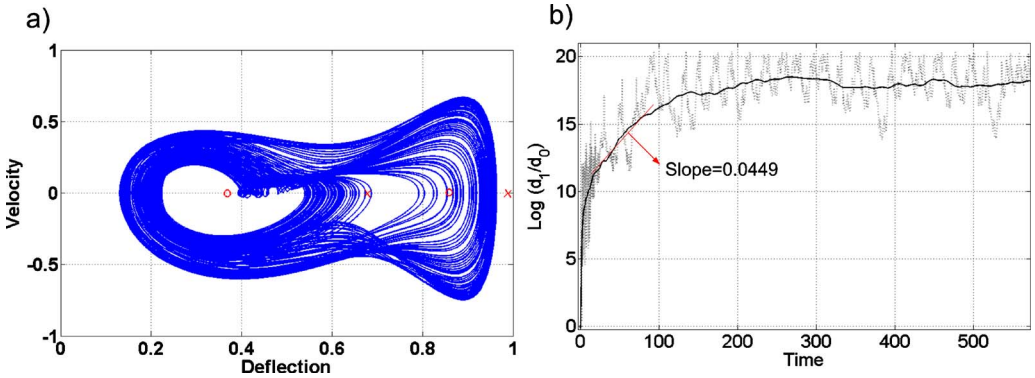

Fig. 20 (*a*) Phase portrait and (*b*) Lyapunov exponent of the two-well chaotic attractor when $V_{ac}=4$ V and $\Omega=1.081$

by the circuit to produce the desired voltage difference between the two electrodes for deriving the beam chaotically.

The chaotic oscillator presented opens the door to a range of applications since the chaotic attractors are bounded, well developed, active, and existed over a wide range of control parameters. These applications include secure communication and enhanced resolution sensing.

Acknowledgment

This research was financially supported by a Postgraduate Scholarship from the Natural Sciences and Engineering Research Council of Canada (NSERC).

References

[1] Epureanu, B. I., Tang, L. S., and Paidoussis, M. P., 2004, "Exploiting Chaotic Dynamics for Detecting Parametric Variations in Aeroelastic Systems," AIAA J., **42**(4), pp. 728–735.
[2] Epureanu, B., and Yin, S.-H., 2004, "Identification of Damage in an Aeroelastic System Based on Attractor Deformations," Comput. Struct., **82**(31–32), pp. 2743–51.
[3] Epureanu, B. I., Yin, S. H., and Derriso, M. M., 2005, "High-Sensitivity Damage Detection Based on Enhanced Nonlinear Dynamics," Smart Mater. Struct., **14**(2), pp. 321–327.
[4] Ghafari, S., 2007, "A Fault Diagnosis System for Rotary Machinery Supported by Rolling Element Bearings," Ph.D. thesis, University of Waterloo, Waterloo, ON.
[5] Yin, S.-H., and Epureanu, B., 2007, "Experimental Enhanced Nonlinear Dynamics and Identification of Attractor Morphing Modes for Damage Detection," ASME J. Vibr. Acoust., **129**(6), pp. 763–770.
[6] Basso, M., Giarré, L., Dahleh, M., and Mezic, I., 1998, "Numerical Analysis of Complex Dynamics in Atomic Force Microscopes," Proceedings of the IEEE International Conference on control Applications, Trieste, Italy, pp. 1026–1030.
[7] Ashhab, M., Salapaka, M., Dahleh, M., and Mezic, I., 1999, "Melnikov-Based Dynamical Analysis of Microcantilevers in Scanning Probe Microscopy," Nonlinear Dyn., **20**(3), pp. 197–220.
[8] Ashhab, M., Salapaka, M., Dahleh, M., and Mezic, I., 1999, "Dynamical Analysis and Control of Microcantilevers," Automatica, **35**(10), pp. 1663–1670.
[9] Lee, S. I., Howell, S. W., Raman, A., and Reifenberger, R., 2002, "Nonlinear Dynamics of Microcantilevers in Tapping Mode Atomic Force Microscopy: A Comparison Between Theory and Experiment," Phys. Rev. B, **66**(11), p. 115409.
[10] Raman, A., and Hu, S., 2006, "Chaos in Dynamic Atomic Force Microscopy," 2006 International Symposium on Nonlinear Theory and Its Applications, Bologna, Italy, pp. 911–914.
[11] Jamitzky, F., Stark, M., Bunk, W., Heckl, W., and Stark, R., 2006, "Chaos in Dynamic Atomic Force Microscopy," Nanotechnology, **17**(7), pp. S213–S220.
[12] Bienstman, J., Vandewalle, J., and Puers, R., 1998, "Autonomous Impact Resonator: A New Operating Principle for a Silicon Resonant Strain Gauge," Sens. Actuators, A, **66**(1–3), pp. 40–49.
[13] Wang, Y. C., Adams, S. G., Thorp, J. S., MacDonald, N. C., Hartwell, P., and Bertsch, F., 1998, "Chaos in MEMS, Parameter Estimation and Its Potential Application," IEEE Trans. Circuits Syst., I: Fundam. Theory Appl., **45**(10), pp. 1013–1020.
[14] De, S. K., and Aluru, N., 2006, "Complex Nonlinear Oscillations in Electrostatically Actuated Microstructures," J. Microelectromech. Syst., **15**(2), pp. 355–369.
[15] DeMartini, B., Butterfield, H., Moehlis, J., and Turner, K., 2007, "Chaos for a Microelectromechanical Oscillator Governed by the Nonlinear Mathieu Equation," J. Microelectromech. Syst., **16**(6), pp. 1314–1323.
[16] Zhang, Y., Wang, Y. S., Li, Z. H., Huang, Y. B., and Li, D. C., 2007, "Snap-Through and Pull-In Instabilities of an Arch-Shaped Beam Under an Electrostatic Loading," J. Microelectromech. Syst., **16**(3), pp. 684–693.
[17] Krylov, S., 2007, "Lyapunov Exponents as a Criterion for the Dynamic Pull-In Instability of Electrostatically Actuated Microstructures," Int. J. Non-Linear Mech., **42**(4), pp. 626–642.
[18] Krylov, S., Ilic, B. R., Schreiber, D., Seretensky, S., and Craighead, H., 2008, "The Pull-In Behavior of Electrostatically Actuated Bistable Microstructures," J. Micromech. Microeng., **18**(5), p. 055026.
[19] Das, K., and Batra, R. C., 2009, "Pull-In and Snap-Through Instabilities in Transient Deformations of Microelectromechanical Systems," J. Micromech. Microeng., **19**(3), p. 035008.
[20] Rhoads, J. F., Shaw, S. W., Moehlis, J., Demartini, B. E., Turner, K. L., and Zhang, W., 2005, "Nonlinear Response of Parametrically-Excited MEMS," DETC2005: ASME International Design Engineering Technical Conferences

and Computers and Information in Engineering Conference, Vol. 1A, pp. 453–461.
[21] Zhang, W.-M., and Meng, G., 2007, "Nonlinear Dynamic Analysis of Electrostatically Actuated Resonant MEMS Sensors Under Parametric Excitation," IEEE Sens. J., **7**(3), pp. 370–380.
[22] Liu, S., Davidson, A., and Lin, Q., 2004, "Simulation Studies on Nonlinear Dynamics and Chaos in a MEMS Cantilever Control System," J. Micromech. Microeng., **14**(7), pp. 1064–1073.
[23] Nayfeh, A. H., Younis, M. L., and Abdel-Rahman, E. M., 2005, "Reduced-Order Models for MEMS Applications," Nonlinear Dyn., **41**(1–3), pp. 211–236.
[24] Towfighian, S., Abdel-Rahman, E. M., and Heppler, G. R., 2008, "Static and Dynamic Analysis of a Bistable Micro-Actuator," Proceedings of the ASME International Mechanical Engineering Congress and Exposition, Boston, MA, pp. 1–11.
[25] Zhang, Y., and Zhao, Y., 2006, "Numerical and Analytical Study on the Pull-In Instability of Micro-Structure Under Electrostatic Loading," Sens. Actuators, A, **127**(2), pp. 366–380.
[26] Lu, M. S.-C., and Fedder, G. K., 2004, "Position Control of Parallel-Plate Microactuators for Probe-Based Data Storage," J. Microelectromech. Syst., **13**(5), pp. 759–769.
[27] Nayfeh, A., Younis, M., and Abdel-Rahman, E., 2007, "Dynamic Pull-In Phenomenon in MEMS Resonators," Nonlinear Dyn., **48**(1–2), pp. 153–63.
[28] Najar, F., Nayfeh, A. H., Abdel-Rahman, E. M., Choura, S., and El-Borgi, S., "Nonlinear Analysis of MEMS Electrostatic Microactuators: Primary and Secondary Resonances of the First Mode," ASME J. Vibr. Acoust., in press.
[29] Moon, F., 1992, *Chaotic and Fractal Dynamics*, Wiley-Interscience, New York.